Chemical Engineering Journal 524 (2025) 168944

Contents lists available at ScienceDirect

Chemical Engineering Journal

journal homepage: www.elsevier.com/locate/cej

3D printed electrochemical sensors with femtosecond laser treatment for cellphone-based portable detection

Yan Dou [a], Kewei Li [b], Haofan Sun [a], Kun Bi [a], Chenyang Zhu [b], Zuanyu Chen [a], Kailong Jin [a], Wonmo Kang [a], Xin Zhao [b,*], Qiong Nian [a,*]

[a] School of Engineering for Matter, Transport and Energy, Arizona State University, Tempe, AZ, 85287, USA
[b] Department of Mechanical Engineering, Clemson University, Clemson, SC, 29634, USA

ARTICLE INFO

Keywords:
3D-printed electrochemical sensors
Femtosecond laser treatment
Copper-based catalysts
Hydrogen peroxide sensing
Potassium ion-selective electrode

ABSTRACT

3D printing technologies offer a promising approach for fabricating electrochemical sensors due to their ease of operation, design flexibility, rapid prototyping, minimal waste, and low cost. However, the printed electrode surfaces typically lack the ideal electrochemical activity needed for sensitive detection. Here, we introduce a novel process called Copper-Driven Laser Graphitization (CDLG), which leverages copper catalysis and femtosecond laser treatment to achieve graphitization of polycaprolactone (PCL). The surface morphology of CDLG-modified electrodes was characterized by SEM, while EDS, XPS, and Raman spectroscopy were used to analyze changes in surface chemical composition. Electrochemical properties, including sensor performance, were evaluated through cyclic voltammetry, electrochemical impedance spectroscopy, amperometry and potentiometric measurement. Results show that CDLG-modified 3D-printed electrodes exhibit a more than six-tyfold increase in sensitivity compared to unmodified printed surfaces, as demonstrated by amperometric measurements of hydrogen peroxide (H_2O_2). Meanwhile, when fabricated into a potassium ion-selective electrode, the CDLG-modified electrode exhibits near-Nernstian behavior for K^+ detection. Furthermore, the 3D-printed electrochemical device can be coupled with a portable smartphone potentiostat, enabling more convenient detection applications. These findings highlight the potential of CDLG to advance 3D-printed electrochemical sensor fabrication, opening new avenues for future sensor designs, expanded applications, and device integration.

1. Introduction

In recent years, 3D-printed electrochemical sensors have attracted growing attention due to their versatile applications across various fields, including clinical analysis [1], environmental monitoring [2], and fouling detection [3]. Among the different 3D printing techniques, Fused Deposition Modeling (FDM) stands out as one of the most cost-effective and widely adopted 3D printing techniques, making it especially attractive for the fabrication of electrochemical sensors [4,5]. The use of FDM in this field offers numerous advantages, including scalable digital production, automated electrode encapsulation, and the creative flexibility to meet specific design requirements [6]. Moreover, FDM supports effective device integration, as illustrated by advancements such as multi-sensor compatible 3D-printed electrochemical cells for drug screening [7], fluidic 3D-printed electrochemical microcells for heavy metal analysis [8], and smartphone-addressable 3D-printed electrochemical rings for nonenzymatic glucose monitoring in human sweat [9]. It can be even combined with screen printing technologies to assemble open source potentiostat for wireless electrochemical detection using smartphones [10]. These innovations highlight the versatility and applicability of FDM fabricated electrochemical sensors in diagnostics [11,12], environmental monitoring [2,13], and industrial analysis [14,15].

When utilizing FDM to directly fabricate electrochemical sensors, one of the key steps is the printing of both electrically conductive and electrochemically sensitive electrodes, which currently faces two technical obstacles. First, currently available FDM filaments usually have insufficient electrical conductivity because of a large proportion of non-conductive thermoplastics contained in these filaments to ensure acceptable FDM printability. To tackle this issue, recent research efforts have explored carbon-based conductive filaments, which focus on incorporating high concentrations of conductive carbon fillers (graphite

* Corresponding authors.
E-mail addresses: xzhao5@clemson.edu (X. Zhao), qiong.nian@asu.edu (Q. Nian).

https://doi.org/10.1016/j.cej.2025.168944
Received 9 June 2025; Received in revised form 11 August 2025; Accepted 24 September 2025
Available online 26 September 2025
1385-8947/© 2025 Elsevier B.V. All rights are reserved, including those for text and data mining, AI training, and similar technologies.

[16], graphene [17], carbon black [18], carbon nanofibers [19], carbon nanotubes [20], etc.) into thermoplastic polymers (PLA, ABS, polystyrene, polypropylene, polyethylene terephthalate glycol-modified, Nylon, etc.) [21]. For example, Kwok et al. reported a conductive filament using carbon black filler in polypropylene polymeric matrix, achieving volumetric resistivity of 0.5 Ω·cm [22]. Commercially available filaments, such as graphene filled PLA (sold by Black Magic 3D) and carbon black filled PLA (sold by Proto-pasta), exhibit volumetric resistivities of 0.6 Ω·cm and 30 Ω·cm, respectively [23]. Similarly, introducing metallic components into polymer matrices is another strategy to enhance filament conductivity. However, directly incorporating metal microparticles into polymer hosts often fails to form continuous conductive pathways due to poor interparticle contact, and can severely deteriorate the mechanical integrity and printability of the filament. Moreover, the high density and thermal conductivity mismatch between metal particles and polymeric carriers create additional processing challenges during FDM printing, such as nozzle clogging or poor layer adhesion [24]. Therefore, achieving effective electrical percolation in metal-polymer composites typically requires the use of specially engineered nanostructures. To this end, recent advances have turned to the integration of metal nanowires—particularly silver (Ag) and copper (Cu)—as promising candidates to establish continuous conductive networks within the polymer phase. For example, Tae Hwan Lim et al. utilized melt-spinning to fabricate polymer/metal/CNT composite fibers with high conductivities ranging from 4.1 to 7.2 $\times$ 10^{-2} S/cm [25]. Mutya A. Cruz et al. synthesized Cu—Ag core–shell nanowires, enabling the production of a highly conductive polymer filament with a remarkably low resistivity of 0.002 Ω·cm [26]. Although notable progress has been made in the development of metal-based conductive filaments, their application in the fabrication of functional electrochemical devices—particularly through direct FDM printing—remains largely unexplored.

The second obstacle is that, when these composite filaments are printed into an electrode, its surface often lack electrochemical activity needed for sensitive detection. This issue arises primarily from high contact resistance due to excessive polymeric material on the surface, which obstructs efficient ion-electron charge transfer. Besides, the fillers themselves may not be equipped with abundant electrochemical active sites, further limiting the electrode sensitivity and overall performance. To address the second obstacle, current research often focuses on using electrochemically active graphene or carbon black to fill composite filaments. Then surface “cleaning” or “activation” is applied to remove residual polymeric materials from electrode surface after FDM printing, thus exposing the carbon fillers for sensitive detection [21]. For instance, Cardoso et al. demonstrated that mechanical polishing and DMF immersion effectively remove excess PLA, exposing graphitic structures on graphene/PLA electrodes for the direct detection of nitrite and uric acid [27]. Similarly, Novotný et al. enhanced electron transfer rates on graphene/PLA electrodes through thermal annealing, which decomposed the PLA binder and enabled the detection of nitroaromatic explosives after electrochemical conditioning [28]. Additionally, Jian et al. utilized cold plasma treatment with O_2 to enhance the electrochemical activity of carbon black/PLA electrodes by removing insulating PLA residues, exposing conductive carbon black sites, and introducing oxygenated functional groups, enabling dopamine detection [29].

Inspired by these efforts on the challenges of FDM-printed electrodes, in this paper, we propose an alternative solution that starts with selecting a composite filament made by copper (with a small amount of silver) and polycaprolactone (PCL) for electrode printing. With copper as the conductive filler, the resistivity of this filament is remarkably low, measuring just 0.006 Ω·cm—two to three orders of magnitude lower than that of carbon-based filaments [23]. Despite the exceptional electrical conductivity of this copper composite filament, printed electrode still lacks electrochemical activity. To solve this issue, we discovered that applying femtosecond laser treatment to the surface of the printed electrode enables the graphitization of PCL. It is hypothesized the graphitization is attributed to ultrafast femtosecond laser breakdown of PCL molecular chains and following copper-catalyzed graphitization. This femtosecond laser treatment, due to its highly efficient digital nature, not only marks the first successful instance of PCL graphitization but also greatly enhances the electrochemical activity of the electrode surface. As a result, our FDM printed electrodes demonstrated a nearly 60-fold improvement in sensitivity for hydrogen peroxide detection after femtosecond laser treatment, achieving a maximum sensitivity of 122.9 $mA{\cdot}M^{-1}{\cdot}cm^{-2}$. By enabling smartphone connectivity, this work also demonstrates that the laser-treated 3D-printed electrochemical sensor can achieve portable detection of hydrogen peroxide and potassium ions in aqueous solutions. Compared to techniques such as aerosol jet printing, inkjet printing and screen printing, which often require complex ink formulations and substrate compatibility constraints [30,31] , this novel method combines FDM 3D printing with digital laser treatment, presenting a transformative manufacturing technology, offering potential for integration of 3D-printed devices to broaden their applicability in future in-field and real-time analysis.

2. Material and methods

2.1. Chemicals and materials

Valinomycin (99 %), bis(2-ethylhexyl) sebacate (DOS), poly(vinyl chloride) (PVC), tetrahydrofuran (THF, 99.9 %), sodium chloride (NaCl), potassium chloride (KCl), phosphate buffered saline (PBS), Silver/silver chloride (60/40) paste and hydrogen peroxide (H_2O_2) solution (30 %) are procured from Sigma-Aldrich. A commercial PCL/Cu conductive filament (electrifi, Multi3D. Inc) in diameter of 1.75 mm is purchased to print the electrodes and devices. A natural PCL filament is purchased from 3D4MAKERS.COM. To print the insulating packaging for the electrodes and devices, PLA filaments in diameter of 1.75 mm are purchased from Creality 3D Inc. The 3D printer utilized to print the above filaments is Creality Ender-3 pro (Creality 3D. Inc). The printer is upgraded from a single extruder to a dual extruder (Ender IDEX) using the extra parts supplied by SEN 3D. Inc. for simultaneous printing and packaging of electrodes and devices. Both nozzles of the dual extruder are in a diameter of 0.4 mm.

2.2. Electrode and device fabrication

Using Computer-aided design (CAD) software SOLIDWORKS, the full-size models of electrodes and devices with external packaging are created and saved as single stereolithography (STL) files. Then, the STL models are sliced into multiple layers to generate G-code files by using the slicing software Ultimaker Cura. After that, the G-code files are input into the 3D printer with a dual extruder to command the printing of the electrodes and devices with external packaging. The PCL/Cu conductive filament are printed at an extrusion temperature of 175 °C. The external packaging is printed using the PLA filament at an extrusion temperature of 210 °C. And all filaments are printed with a layer height of 0.15 mm, line width of 0.4 mm, and infill density of 100 %.

The electrode structure, measuring 45 mm in length, 5 mm in width, and 1 mm in thickness, is printed using PCL/Cu conductive filament and serves as the electrical conduction component. A 0.5 mm thick encapsulating layer, printed with PLA, encloses the electrodes, precisely defining the sensor’s active region. This designated active area features a circular geometry with a 4 mm radius, corresponding to an approximate planar surface area of 50 mm^2. The printing resolution, layer stacking consistency, and interfacial bonding quality of this fabrication process have been optimized in our previous work [32].

The sensor device consists of five distinct components: two fluidic pipes, three electrodes, a lower container part, and an upper container part. These components are individually designed using SOLIDWORKS and assembled into a complete sensor device in Ultimaker Cura before

being sliced and printed using a dual-extruder 3D printer. The final structure forms a rectangular container with dimensions of 33 mm × 24.5 mm × 16 mm and a wall thickness of 2 mm. Two fluidic pipes serve as inlet and outlet channels for liquid flow at both ends of the container. Three electrodes are embedded at the bottom of the container, with a circular active area of 4 mm in radius exposed on the lower surface. Further details of the device design are provided in Figs. S1 and S2.

2.3. Femtosecond laser processing

Subsequent to printing, the electrodes undergo processing using a 1030 nm femtosecond laser produced by a Yb: KGW femtosecond laser system (PHAROS by Light Conversion). The linearly polarized laser has a pulse duration of 165 fs and a Gaussian beam profile. A laser scan head (intelliSCAN by SCANLAB) is utilized to focus the laser on the electrodes and create a circular scanning region that encompasses the designated active area. The laser fluence is varied (1 J/cm^2, 5 J/cm^2, 10 J/cm^2, 15 J/cm^2, 20 J/cm^2, and 25 J/cm^2) to assess its effect on graphitization, while the repetition rate and overlapping ratio are maintained at 10 kHz and 85 %, respectively. Noble gas (Ar) is introduced during laser scanning to eliminate the ablated big particles and shield the treated surface from oxygen in the environment.

2.4. Potassium ion selective electrode (ISE) synthesis

Laser-scribed electrodes are transformed into potassium ISEs by depositing a potassium-selective membrane onto the circular section of the CDLG electrode. The membrane cocktail comprises 1.0 wt% valinomycin, 66 wt% DOS, and 33 wt% PVC, dissolved in 5 mL of THF at a concentration of 15 wt%. A 50 μL aliquot of this cocktail is drop-coated onto the electrodes and air-dried for 6 h.

2.5. Characterization

The microstructures of the PCL/Cu and CDLG substrate surfaces are examined using a Field Emission Scanning Electron Microscope (FEI Nova 200 NanoLab, Thermo Fisher Inc.). FE-SEM images are captured in secondary electron (SE) mode with an accelerating voltage of 5 kV and a beam current of 1.6 nA, maintaining a working distance of 5 mm from the field emitter source aperture. Additionally, an EDS detector is employed to determine the chemical composition and distribution across the samples.

Confocal Raman microscopy is performed using an Acton 300 LN2 spectrometer. The Raman signal is isolated from laser excitation using an Ondax SureBlock™ ultranarrow-band notch filter combined with two OptiGrate notch filters. The samples are analyzed with a 532 nm wavelength laser, powered by a 150 mW Coherent Sapphire SF laser. Using Raman spectroscopic data, the crystalline size along the a-axis (L_a) can be calculated from the ratio of the integrated intensity of the G peak (I_G) and D peak (I_D). The L_a value can be obtained using the following equation [33]:

$$L_a = \left(2.4 \times 10^{-10}\right) \times \lambda^4 \times \frac{I_G}{I_D}$$

The X-ray Photoelectron Spectroscopy (XPS) spectra of the electrode surfaces are acquired using a Kratos Axis Supra+ X-ray Photoelectron Spectrometer, equipped with dual monochromatic Al/Ag sources (Al K-alpha 1486.6 eV and Ag L-alpha 2984.2 eV). Binding energy survey scans are generated by measuring the photoelectron energies of the constituent elements and subtracting the excitation energy.

Cyclic voltammetry (CV), Electrochemical Impedance Spectroscopy (EIS), and amperometric sensing are conducted using a CHI Instruments potentiostat (660 series) configured in a three-electrode setup. The PCL/Cu or CDLG 3D-printed electrodes serve as the working electrode, Ag/AgCl (1 M KCl) is used as the reference electrode, and a platinum wire acts as the counter electrode. For EIS and EIS tests, 1× PBS with 0.1 mM H_2O_2 is used as the electrolyte to assess electrochemical activity and impedance. EIS measurements are performed at open-circuit voltage over a frequency range of 1 MHz to 0.1 Hz with an amplitude of 5 mV. The equivalent circuit fitting and the corresponding C_{dl} values were obtained using ZView software.

For H_2O_2 sensing, all electrodes are submerged in a 10 mL test vial containing the electrolyte, with the solution continuously stirred at 600 rpm using a 0.5 cm magnetic stir bar. Incremental increases in hydrogen peroxide concentration are achieved by pipetting 10 μL of 100 mM H_2O_2 solution into the test vial in ten successive additions. During the experiments, a working potential of 0.1 V is maintained between the working and counter electrodes.

For potentiometric measurements, CDLG ISEs act as the working electrode. Before electrochemical testing, the electrodes are conditioned in a 0.01 M KCl solution for 24 h and stored dry at room temperature between experiments. The analytical performance of the potassium ISEs is evaluated in a KCl solution over a concentration range of $10^{-5.5}$ to 10^{-2} M. Additionally, a water layer test is conducted by exposing the CDLG ISE to a 0.01 M KCl solution for 4 h, followed by a 0.01 M NaCl solution for 2.5 h, and then returning to the initial KCl solution for 8.5 h while continuously recording the potential. The limit of detection (LOD) is determined using the three-sigma method (3σ).

2.6. Measurement

For device measurements, a Sensit Smart potentiostat (Palmsens, Houten, Netherlands), controlled via the PStouch Android app, is employed. The two laser-scribed areas function as both the working and counter electrodes, while Ag/AgCl paint serves as the reference electrode. When the H_2O_2 test solution enters the detection chamber, chronoamperometry is performed at a potential of 0.1 V for 100 s to quantify H_2O_2 levels. Similarly, when PBS samples are introduced into the device, potentiometric measurements are carried out to determine potassium ion K^+ concentrations.

For the detection of H_2O_2, an amperometric sensing mechanism is employed. At an applied potential of −0.1 V vs. Ag/AgCl, H_2O_2 undergoes electrochemical reduction on the carbon-based working electrode surface, producing a Faradaic current proportional to the H_2O_2 concentration. The magnitude of the steady-state current thus reflects the analyte level.

For K^+ detection, a potentiometric mechanism based on ISEs is used. The sensor operates under open-circuit conditions, where a selective membrane containing valinomycin facilitates K^+-selective ion exchange. The resulting potential difference, measured between the working electrode and the reference electrode (Ag/AgCl), follows the Nernst equation and varies logarithmically with K^+ activity.

2.7. Simulation

Local temperature field is essential for evaluating the graphitization process. Consequently, a 2D axisymmetric finite element model is constructed using COMSOL Multiphysics to investigate the local temperature distribution. During the ultrafast laser-matter interaction process, the laser energy is first absorbed by free electrons and then transferred into the lattice system via the electron-lattice interactions. The local (electron and lattice) temperatures can be described and captured by the two-temperature model (TTM), with the governing equations shown below [34,35]:

$$C_e \frac{\partial T_e}{\partial t} = \nabla(k_e \nabla T_e) - G(T_e - T_l) + S$$

$$C_l \frac{\partial T_l}{\partial t} = \nabla(k_l \nabla T_l) + G(T_e - T_l)$$

Here T_e and T_l are transient temperatures of electron and lattice systems. k_e and k_l denote thermal conductivities of electron and lattice

systems. C_e and C_l are electron and lattice heat capacity and G represents the electron-lattice coupling coefficient. S is the laser energy and t is time.

This model represents the printed electrode as a copper slab structure overlaid with an imaginary optical absorbing layer composed of PCL. The thermal impact of the imaginary PCL layer is minimal due to its low thermal decomposition temperature. Initial electron and lattice temperatures are set to room temperature (293.15 K). The axisymmetric boundary condition is implemented on the left surface, whereas the adiabatic boundary condition is applied to both the right and bottom surfaces. The upper surface is designated as an open boundary to account for thermal radiation and material ablation.

3. Results and discussion

3.1. Copper-driven laser graphitization

As shown in Fig. 1a, the PCL/Cu composite filament is selected for the 3D printing of sensor electrodes using FDM technology. FTIR spectroscopy was performed to characterize the chemical structure of the PCL/copper composite electrode surface (Fig. S3). The spectrum exhibits characteristic absorption bands of PCL, including the strong carbonyl (C=O) stretching vibration at ~1720 cm^{-1}, associated with the ester group in the polymer backbone. The asymmetric and symmetric CH_2 stretching vibrations appear at ~2943 cm^{-1} and ~ 2865 cm^{-1}, respectively, while the CH_2 bending and scissoring modes are observed at ~1465 cm^{-1} and ~ 1418 cm^{-1}. Additionally, the C–O–C stretching vibration of the ester group is identified in the range of 1240–1160 cm^{-1} [36]. These characteristic peaks confirm the presence of PCL as the polymer matrix in the composite filament, indicating that the melt-extrusion process used for filament fabrication preserved the fundamental chemical structure of PCL without detectable degradation. After printing, femtosecond laser scribing is applied to the electrode surface under ambient conditions. Driven by the catalytic effect of copper and the influence of the laser, the PCL spontaneously transforms into graphene on the copper surface, a phenomenon we term as Copper-Driven Laser Graphitization (CDLG). The mechanism of CDLG is fundamentally different from traditional laser-induced graphene (LIG) [37]. In LIG, polymers are photothermally converted to graphene by pulsed CO_2 laser irradiation, but the selection of suitable carbon precursors is limited to materials containing aromatic rings or hexagonal structures. For example, polyimide (PI) and poly(etherimide) [38], due to their aromatic and imide repeat units, as well as lignin-containing precursors with cross-linked aromatic structures [39], can form LIG. In contrast, ablated polymers such as PCL and PLA, commonly used in FDM 3D printing, tend to depolymerize and ablate under laser processing rather than yielding graphene due to their low melting points and lack of aromatic structures [40].

We propose that the underlying mechanism of CDLG involves two critical factors: the use of femtosecond pulsed lasers and the catalytic role of copper. Femtosecond lasers, with their ultrashort pulse duration and high peak power, are capable of cold ablation (as shown in Fig. 1a right), which breaks chemical bonds to ionize atoms and leaves low residual heating in the material [41,42]. This makes them highly effective for processing the PCL polymer in our electrodes, leading to carbon bonds breaking and carbon radicals/ions formation [43]. In addition to the unique femtosecond laser effect, the catalytic properties of copper play a pivotal role in the CDLG process, akin to its function in Chemical Vapor Deposition (CVD), where pyrolyzed carbon sources absorb onto copper surface to form graphene lattice structure [44,45]. In CDLG, copper nanocrystals serve as catalytic templates with excellent efficiency to absorb the ionized carbon atoms and then form graphitic skeletons.

In summary of our proposed CDLG mechanisms as shown in Fig. 1b, when femtosecond laser irradiates the surface of PCL/Cu electrodes, the ultrashort laser pulses deliver massive, localized energy into PCL through multiphoton absorption, rapidly exciting and ejecting electrons. This leads to breaking of chemical bonds within the polymer chains, and then decomposition of the polymer into reactive carbon species, which eventually absorb onto the copper surface and reorganize into sp^2-hybridized carbon structures, i.e., graphene structure. Notably, Fig. S4 presents the TEM image and corresponding FFT pattern of the copper cross-section after femtosecond laser treatment. It reveals the formation of nanocrystals on the copper surface. This phenomenon arises because femtosecond laser pulses induce rapid heating and ultrafast cooling, which suppresses grain growth and promotes non-equilibrium phase transitions. In addition, the high-pressure shock waves generated during laser irradiation introduce significant mechanical stress, leading to severe plastic deformation and dynamic recrystallization. These combined effects refine the grain structure and result in the formation of stable surface nanocrystals.

To elucidate the influence of femtosecond laser irradiation on graphene formation, the evolution of lattice temperature induced by a femtosecond laser pulse (pulse duration: 165 fs) is investigated using the two-temperature model (TTM), as illustrated in Fig. 1c. The laser pulse propagates along the negative z-direction and impinges upon the PCL/copper composite at the z = 0 nm plane. Immediately following irradiation, rapid heating occurs, initiating intense thermal decomposition of the PCL layer, phase explosion within the copper substrate, and subsequent material ablation confined to a narrow region—an event characterized as “cold ablation.” The ablation front is distinctly highlighted, marking the formation and progression of the ablation crater during and subsequent to the ultrafast laser processing. As thermal energy dissipates from the ablation front, copper undergoes resolidification, facilitating the reorganization and nucleation of absorbed active carbon species on its surface. This nucleation process initiates the growth of high-quality graphene within an optimized temperature window ranging from 1357.15 K down to 573.15 K [46–49]. The identification of this graphene formation window, outlined in Fig. 1c, validates the capability of ultrafast laser irradiation to effectively induce graphene growth, thereby supporting the proposed CDLG mechanism.

To confirm the indispensable role of copper in the CDLG process, we have designed a controlled experiment where PCL is thermally pressed onto a copper foil, and its surface is then subjected to femtosecond laser scribing. Supplementary Fig. S5 depicts a sample of PCL substrate which is laser-scribed directly, as well as PCL thermally pressed onto copper foil and then laser-scribed. The images clearly show that the color of the PCL substrate changes from white to light gray after laser scribing, while the sample of PCL coating on copper foil turns from white to black. Furthermore, Raman spectroscopy is performed on the PCL, the PCL/Cu composite, laser-scribed PCL, and laser-scribed PCL coated on copper foil. As depicted in Fig. 1d, characteristic peaks of graphitization, the D peak at ~1350 cm^{-1} (indicative of defect regions, also known as the disorder or defect band) and the G peak at ~1580 cm^{-1} (indicative of the planar configuration of sp^2 bonded carbons) [50], are only observed in the laser-scribed PCL coating on copper foil. This clearly demonstrates that copper is essential for the successful graphitization of PCL subjected to femtosecond laser treatment. Similarly, when the same experiment is conducted with PLA, the CDLG process is also successfully achieved (Fig. S6). Given that both PCL and PLA are widely used materials for 3D printing, CDLG can undoubtedly be combined with FDM 3D printing. For the electrodes printed using the Cu/PCL filament, the corresponding Raman spectra, as shown in the upper right corner of Fig. 1d, exhibit not only prominent D and G bands but also a weak 2D peak at ~2700 cm^{-1}, indicative of a second-order Raman scattering feature. This observation suggests that the intimate contact between Cu and PCL within the composite filament enhances the catalytic effect of copper, thereby promoting the formation of low-layer-number graphene with limited crystallinity.

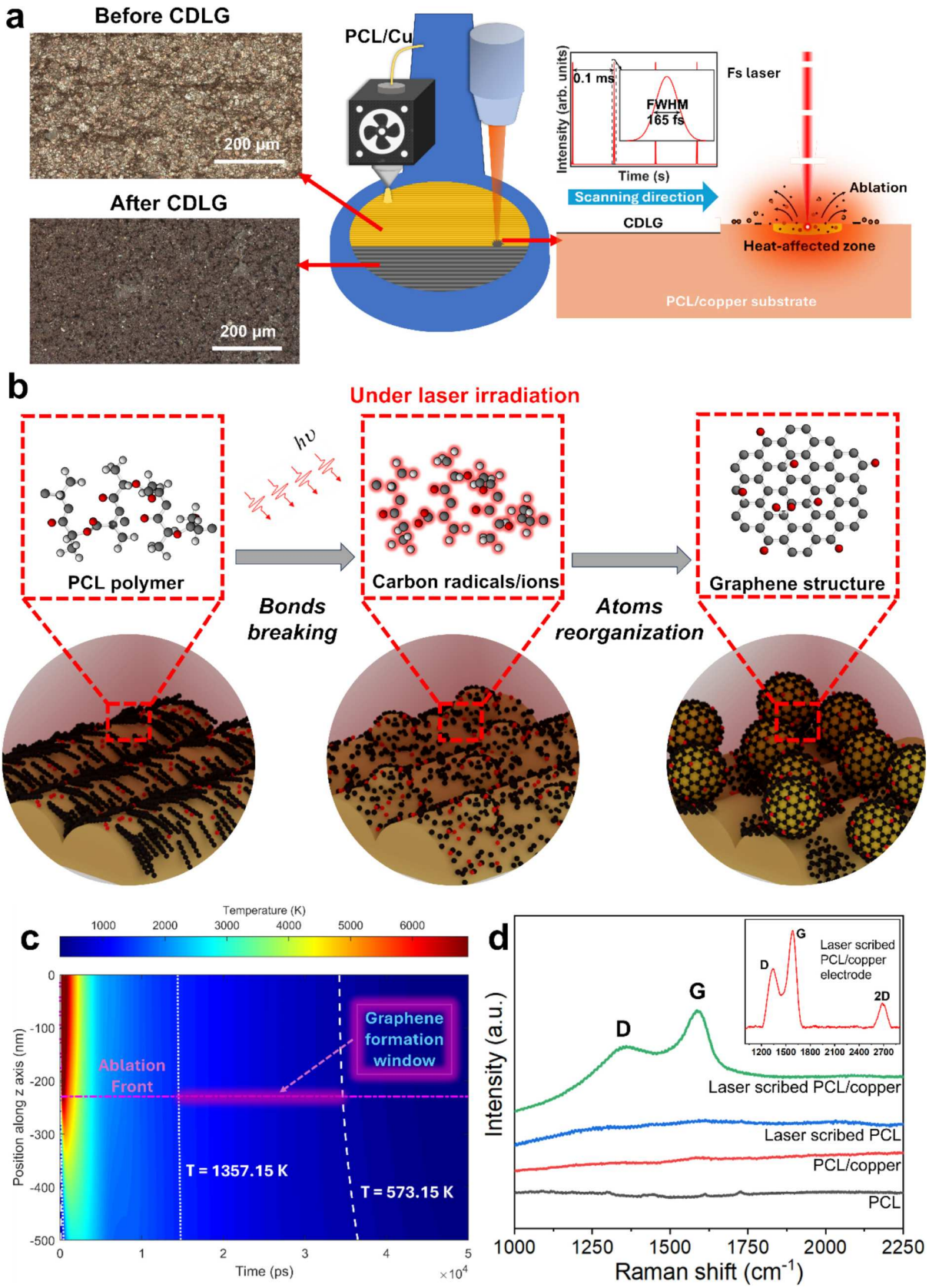

Fig. 1. (a) Schematic of 3D printing and femtosecond pulsed laser surface treatment, and photographs of electrodes before and after laser processing. (b) Schematic of the synthesis process of CDLG from biodegradable polymer with the help of copper. (c) Simulated lattice temperature profile with laser fluence at 15 J/cm^2 and highlighted graphene formation window. (d) Representative Raman spectrum of laser scribed PCL/Cu substrate, laser scribed PCL, PCL/Cu, PCL and laser scribed PCL/Cu electrode.

3.2. Simulation

Graphene fabrication catalyzed by copper through CVD method has been extensively investigated. High temperatures are essential to break down carbon precursors and facilitate carbon diffusion onto copper surfaces, following a surface-mediated growth mechanism [51]. Typically, graphene synthesis via CVD is reported at temperatures ranging from 573.15 K to 1357.15 K [46–49]. In addition to elevated temperatures, sufficient reaction time is critical to enable carbon diffusion and nucleation. Molecular dynamics simulations indicate that hexatomic carbon ring structures generally form within 100 to 200 ps [52,53]. However, excessively prolonged reaction times may promote multilayer graphene formation [52,54] and increase defect densities [55,56], thereby adversely affecting graphene quality. To critically assess the proposed CDLG mechanism, especially regarding the roles of temperature and reaction time, numerical simulations using the two-temperature model (TTM) were performed to study temperature evolution.

As depicted in Fig. 2(a-c), within the initial 500 ps, absorbed laser energy rapidly transfers into the copper substrate, significantly raising both electron and lattice temperatures. The ablation front, defined by the isotherm at 0.9 times copper's critical temperature (0.9Tc = 6926 K), exhibits a constant peak lattice temperature, whereas the highest local electron temperature increases with rising laser fluence. At a fluence of 10 J/cm^2, local temperatures at the ablation front surpass 6500 K, substantially exceeding the decomposition threshold of PCL (~553.15 K). Under these extreme conditions, the catalytic role of copper is rendered ineffective since copper is no longer in its solid state. Graphene formation occurs predominantly during subsequent rapid cooling phases. After 10,000 ps, the localized temperature decreases below 1400 K, favoring the synthesis of high-quality graphene.

As shown in Fig. 2(d), a sufficient reaction duration of approximately 9894 ps is achieved at a fluence of 10 J/cm^2, suitable for graphene formation. Notably, the graphene formation window exhibits a monotonic increase with rising laser fluence. At 15 J/cm^2, the reaction time extends to 20,112 ps, while a fluence of 20 J/cm^2 results in the longest reaction time of 31,422 ps among the three simulated cases. These results indicate that graphene synthesis via CDLG is facilitated by maintaining appropriate temperature and reaction time conditions. Furthermore, the selected laser energy plays a critical role in determining the quality of graphene. While increased fluence supports longer reaction times, it may also lead to higher defect densities due to enhanced plasma generation, alterations in copper morphology and chemical states, and changes in the carbon-to-oxygen ratio—factors not fully captured by the current simulation. Subsequent surface characterizations, including Raman spectrum and XPS analysis, reveal that a laser fluence of 15 J/cm^2 is effective in creating the highest quality of graphene, followed by 10 J/cm^2, while 20 J/cm^2 yields the least. These findings suggest that optimal CDLG formation necessitates a balanced interplay of thermal history, reaction duration, material ablation, and chemical dynamics.

3.3. Surface morphological characterization

Although CDLG can form graphene on the surface under ambient conditions; to elucidate the precise material changes induced by femtosecond laser treatment and minimize the interference of oxygen in elemental analysis, the entire femtosecond laser processing has been conducted in an argon atmosphere. To further investigate the influence of laser fluence on the graphitization of PCL, the surface of the 3D-

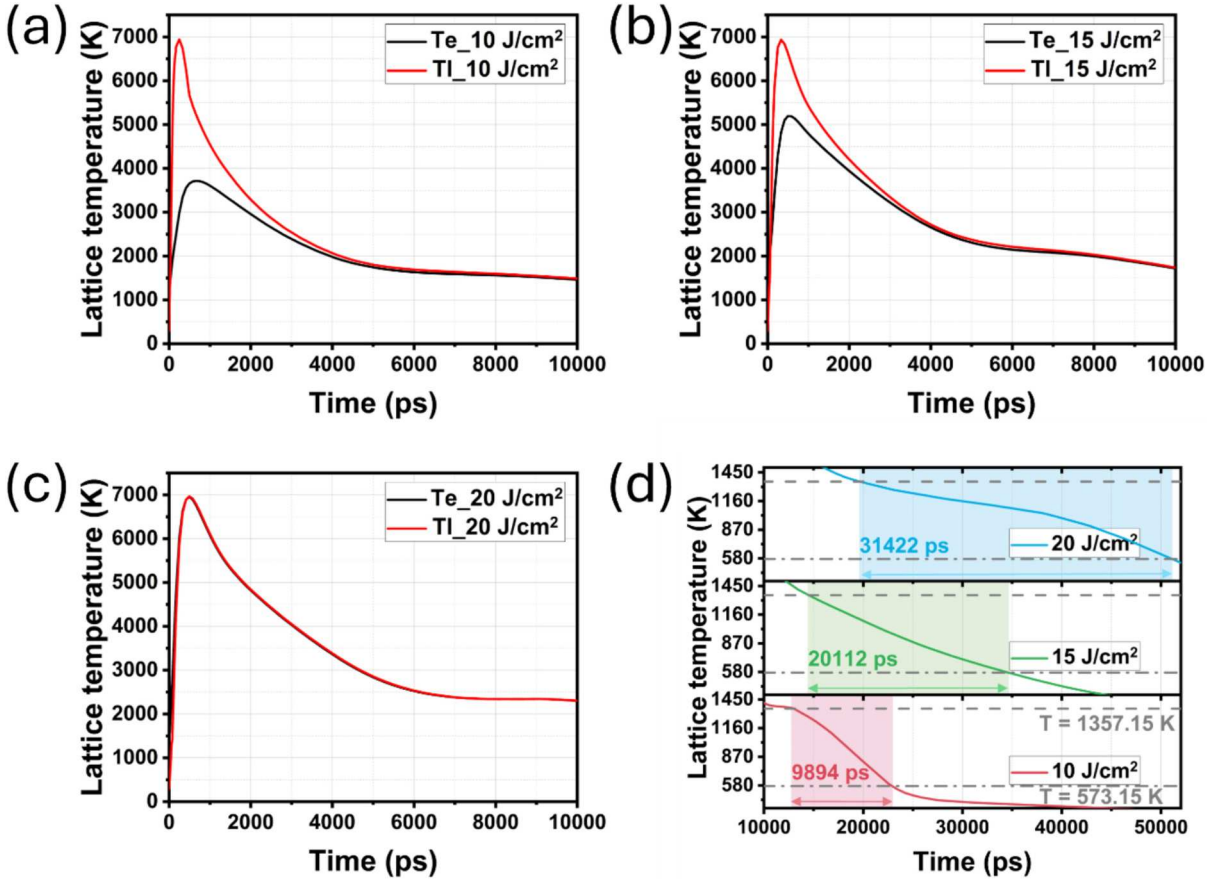

Fig. 2. Simulated electron and lattice temperature at ablation front under laser fluence at (a)10 J/cm^2, (b)15 J/cm^2, (c)20 J/cm^2 and (d) graphene formation window.

printed PCL/Cu composite electrodes is scribed using lasers with fluences of 1 J/cm^2, 5 J/cm^2, 10 J/cm^2, 15 J/cm^2, 20 J/cm^2, and 25 J/cm^2.

The SEM images of the surface at various magnifications clearly demonstrate the morphological evolution of the PCL/Cu composite as a function of laser fluence. As shown in Fig. 3(a,e), the surface of the untreated 3D-printed PCL/Cu composite is characterized by densely packed flakes of varying sizes and shapes. With an increase in laser fluence to 5 J/cm^2, as depicted in Fig. 3(b,f), several surface flakes disintegrate due to the laser energy, while the remaining flakes fuse together. A small number of uniformly distributed nanoscale spherical particles also begin to precipitate on the surface. As the laser fluence further increases, more flakes disintegrate, resulting in a greater deposition of nanoscale spherical particles. At a fluence of 15 J/cm^2 (Fig. 3c, g), the majority of the CDLG composite surface is covered by these nanoparticles, and by 25 J/cm^2 (Fig. 3d,h), the surface is almost entirely enveloped by them. To further investigate the changes in elemental distribution and content of Cu, C, and O on the PCL/Cu composite surface before and after femtosecond laser processing, EDS mapping is employed. Before laser treatment (Fig. 3i), Cu, C, and O are uniformly distributed across the flake-covered surface, with relative atomic ratios of 18.1 %, 79.2 %, and 2.7 %, respectively. After laser treatment at a fluence of 15 J/cm^2 (Fig. 3j), Cu, C, and O are predominantly concentrated on the nanoscale spherical particles, with relative atomic ratios of 44.9 %, 51.8 %, and 3.3 %, respectively. These results indicate partial degradation of the PCL matrix and increased exposure of copper on the surface.

The combined results of SEM and EDS suggest that during femtosecond laser processing, the intense and ultra-short laser pulses generate rapid localized heating, leading to the ablation and melting of the composite material. The high surface tension of molten copper, coupled with the minimal heat diffusion characteristic of femtosecond laser processing, energetically favors the formation of spherical shapes [57]. Additionally, the photothermal effects and mechanical stresses induced by the laser pulses decompose the PCL polymer matrix [58]. This facilitates the redistribution and condensation of copper nanoparticles into nanospheres, a process that becomes more pronounced at higher laser fluences. Simultaneously, the laser fluences, combined with the catalytic properties of copper, create the necessary conditions for carbon graphitization, resulting in the deposition of small graphene sheets on the nanospheres formed during laser irradiation.

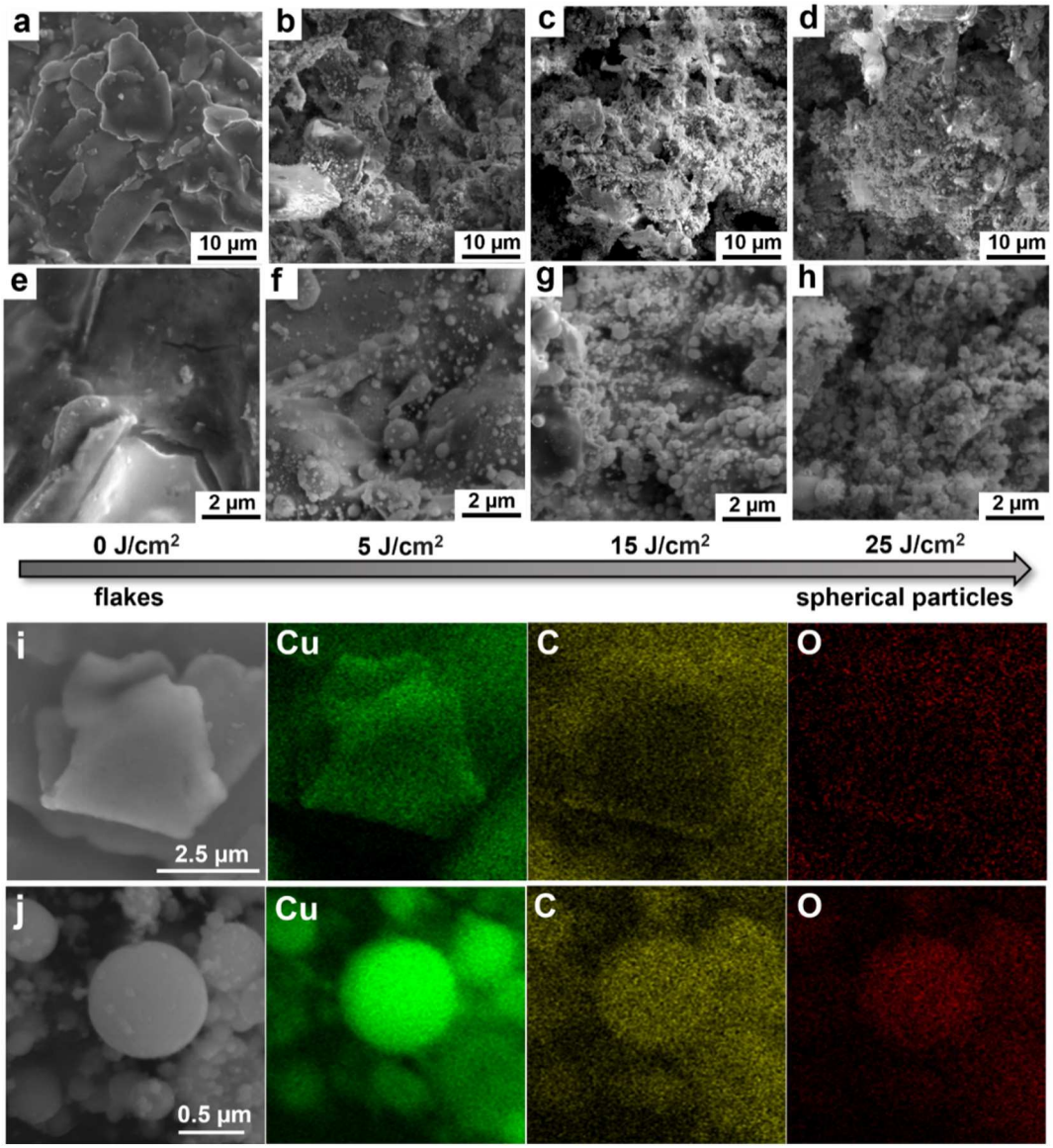

Fig. 3. SEM images of laser-scribed PCL/Cu composites treated with laser fluences of (a,e) 0 J/cm^2, (b,f) 5 J/cm^2, (c,g) 15 J/cm^2, (d,h) 25 J/cm^2. And quantitative EDS element mapping of Cu, C and O of (i) 0 J/cm^2 and (j) 15 J/cm^2.

3.4. Surface composition characterization

To examine the graphene layers and structural characteristics of the CDLG composites, Raman spectroscopy is employed to analyze the samples. The structural defects of graphene, the in-plane vibrations of sp^2 carbon atoms, and the stacking arrangement of carbon atoms in the interlayer are identified by the D peak, G peak, and 2D peak, respectively. As shown in Fig. 4a, the characteristic graphene peaks appear at approximately 1350 cm^{-1} (D peak), 1580 cm^{-1} (G peak), and 2700 cm^{-1} (2D peak), confirming the formation of graphene structures within the CDLG composite under all laser conditions [50]. Moreover, the I_D/I_G ratio is used to evaluate defect density within the graphene structure [59]. As depicted in Fig. 4b, the I_D/I_G ratio shows a direct correlation with increasing laser fluence, reaching its minimum at 15 J/cm^2, indicating the lowest density of graphene defects at this point. Beyond this fluence, the ratio begins to rise, indicating an increased density of graphene defects at higher laser fluences. Similarly, the full width at half maximum (FWHM) of the G peak exhibits the same trend with increasing laser energy; a larger FWHM value suggests a slight increase in the content of dopant atoms, such as oxygen, introduced during the composite photothermal conversion process [60]. Additionally, the I_{2D}/I_G ratios are generally weak, indicating a high concentration of oxygen functional groups and interlayer fractures and distortions in the CDLG structure [61]. The L_a values, calculated from the average I_G/I_D ratio using equation (1) (Experimental Section), are presented in Fig. S7. The L_a increases to approximately 14.4 nm as the laser fluence rises to 15 J/cm^2, which can be attributed to the increased density of the surface copper nanospheres. However, further increases in laser power degrade the quality of the graphene, reducing the L_a to approximately 10.2 nm at 25 J/cm^2, likely due to over-ablation and excessive heating. Overall, CDLG tends to produce smaller-sized graphene structures. This is primarily because the ultrashort femtosecond laser pulses do not provide sufficient time for reactive carbon species to undergo extensive nucleation and diffusion growth. Additionally, the nanoscale copper spheres lack the large, flat surfaces required for the growth of larger graphene sheets.

Fig. 4c presents the XPS survey spectra of PCL/Cu and CDLG composites, highlighting carbon, oxygen, and copper as the primary elements detected. The copper peak in the CDLG composites is significantly higher than that in the PCL/Cu composites, indicating greater exposure of copper on the surface after femtosecond laser treatment, which aligns with the EDS results. Unlike EDS, which can detect elemental composition up to 1 to 2 μm in depth, XPS provides surface analysis at a depth of 1 to 10 nm. This allows for a more precise characterization of the changes in carbon accumulation on the copper nanospheres as a function of laser fluence. Fig. 4d shows the atomic percentages of carbon, copper, and oxygen based on XPS analysis. It can be observed that the surface of the PCL/Cu composites is primarily covered by PCL, with minimal copper exposure. However, upon femtosecond laser treatment, a portion of the PCL decomposes, leading to increased copper exposure on the surface. When the laser fluence increases to 5–15 J/cm^2, the elemental composition stabilizes, suggesting that this range of laser energy does not further degrade the carbon in the CDLG composites. However, when the energy exceeds the 15 J/cm^2 threshold, the atomic

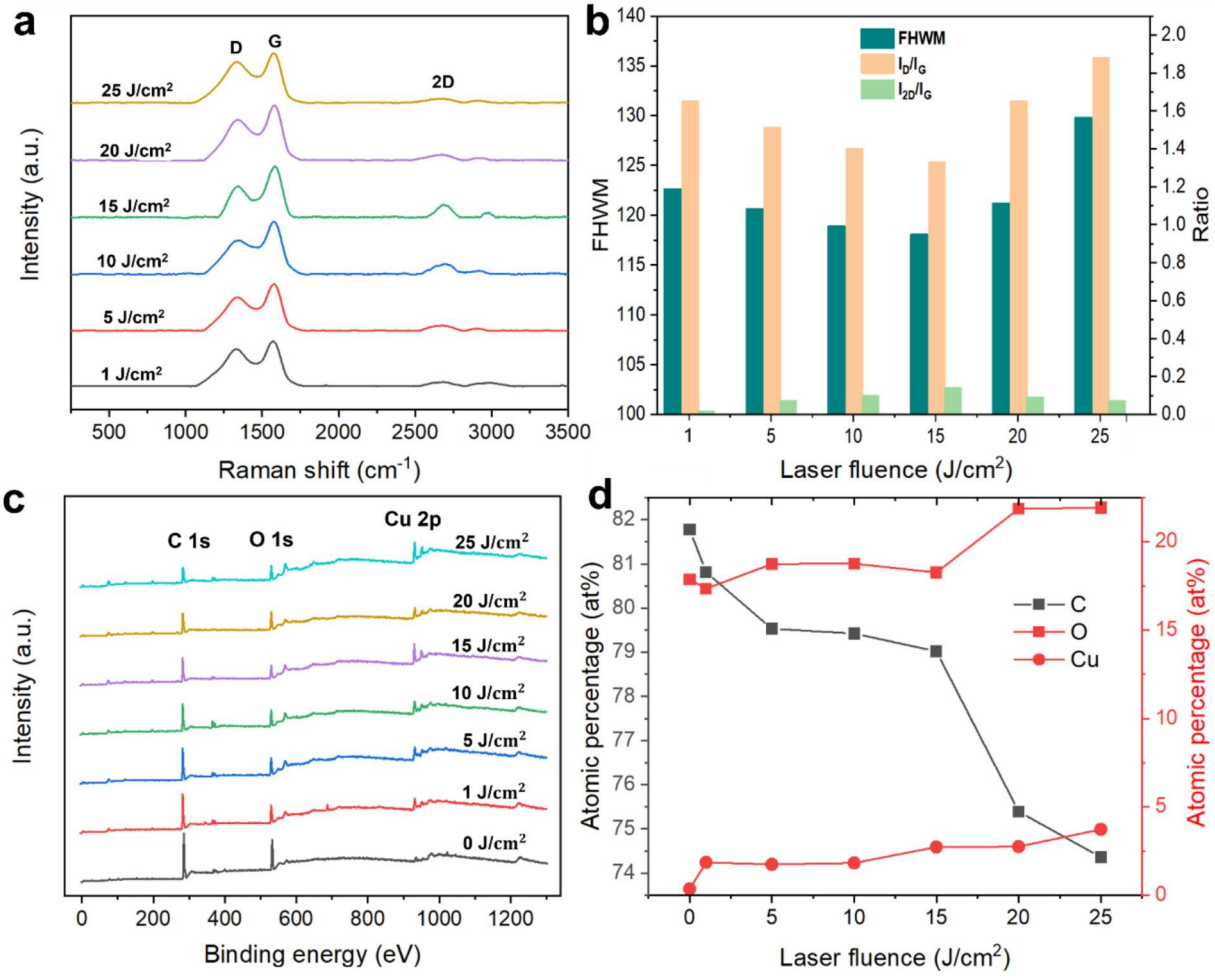

Fig. 4. Characterization of PCL/Cu and CDLG composites. (a) Raman spectra. (b) I_D/I_G, I_{2D}/I_G, and FWHM calculated from Raman spectroscopy data. (c) Survey spectra of XPS test results. (d) Atomic percentages of carbon, oxygen and copper as a function of laser fluences. These values are obtained from XPS.

percentage of carbon sharply decreases, indicating over-ablation and excessive heating further disrupts the graphene structure. This observation is consistent with the Raman spectroscopy results. It is noteworthy that when PCL/Cu composites are processed under ambient conditions, the presence of oxygen in the air exacerbates carbon decomposition (Fig. S8).

Further, the C 1s and Cu 2p XPS spectra are obtained for both PCL/Cu and CDLG composites. The C 1s peak is analyzed by deconvoluting the spectra using Lorentzian peak fitting to identify the constituent components. The PCL/Cu composites primarily exhibit characteristic bonds of PCL, specifically C—C (284.8 eV), C—O (286.1 eV), and C═O (288.8 eV), as shown in Fig. 5a [62]. As the laser fluence gradually increases to 15 J/cm^2 (Fig. 5b), the positions and intensities of the C—O and C═O peaks remain largely unchanged. However, a C═C peak emerges at a binding energy of 284.5 eV, along with a shake-up satellite π–π* peak at 290.2 eV, indicating the formation of aromatic carbon structures [63]. When the laser fluence exceeds 15 J/cm^2 (Fig. 5c), the intensity of the C═C peak decreases, suggesting that excessive laser energy leads to over-ablation of the carbon matrix and the degradation of sp^2-hybridized carbon structures. Additionally, the XPS spectra of the PCL/Cu composites are examined in the Cu 2p region, as shown in Fig. 5d. The strong Cu^{2+} satellite peaks located at 945 and 963 eV indicate the presence of significant CuO on the surface of CDLG [64]. As the laser fluence increases to 10 J/cm^2 (Fig. 5e), CuO remains evident on the CDLG surface. However, when the laser fluence is raised to 15 J/cm^2 and beyond (Fig. 5f), the strong Cu^{2+} satellite peaks disappear. The binding energies for the Cu 2p$_{3/2}$ and Cu 2p$_{1/2}$ peaks are located at 932.6 eV and 952.4 eV, respectively, indicating that CuO has been reduced to Cu. In contrast, when PCL/Cu composites are processed under ambient conditions, Cu^{2+} satellite peaks in the Cu 2p region are still observed at laser fluences of 15 J/cm^2 and above (Fig. S9). This suggests that after CuO is reduced by the laser, some of the Cu reacts with ambient O_2 under the residual heat of laser irradiation to re-form CuO.

Based on the preceding characterization results, it can be concluded that CDLG induces a unique morphology and distinct material properties. Morphologically, the graphene formed by CDLG encapsulates nanoscale copper particles, resulting in a structure that differs significantly from those produced by conventional methods such as CVD or traditional LIG. Unlike CVD-grown graphene, which typically yields large-area, well-ordered crystalline domains, and unlike LIG, which often produces highly porous, foam-like structures, the graphene generated here is limited to nanocrystalline domains tightly bound to the copper nanoparticles. Despite the absence of long-range crystallinity or hierarchical porosity, the resulting structure demonstrates promising electrochemical behavior, as verified by subsequent electrochemical analyses. This indicates that the nanoscale features and the intimate interaction between graphene and copper may play a key role in facilitating effective charge transfer and enhancing the electrode's functional performance.

3.5. *Electrochemical analysis and application*

To investigate the electrochemical activity of CDLG, electrodes are fabricated using PLA filament and PCL/Cu filament with the integrated encapsulation capability of a dual-head 3D printer. The PCL/Cu electrode, designed as a single-channel electrode (marked in yellow, labeled as Y), is encased within a polylactic acid (PLA) package (marked in blue, labeled as B), as illustrated in Fig. 6a. The single-channel electrode measures 45 mm in length, 5 mm in width, and 1 mm in thickness, while the PLA package, with a thickness of 0.5 mm, not only seals the electrodes but also defines the active area. The geometrical surface area of the electrode is approximately 50 mm^2 with a radius of 4 mm. In our previous studies, this printed single-channel electrode demonstrates excellent sealing properties, ensuring that the electrolyte does not penetrate the PLA layers during operation in an electrolyte solution [32]. After printing, to maintain consistency with previous characterization experiments, the PCL/Cu 3D-printed electrodes are treated with different laser fluences under an argon atmosphere using femtosecond laser processing to produce CDLG 3D-printed electrodes.

EIS is then employed to evaluate the impedance of the PCL/Cu and

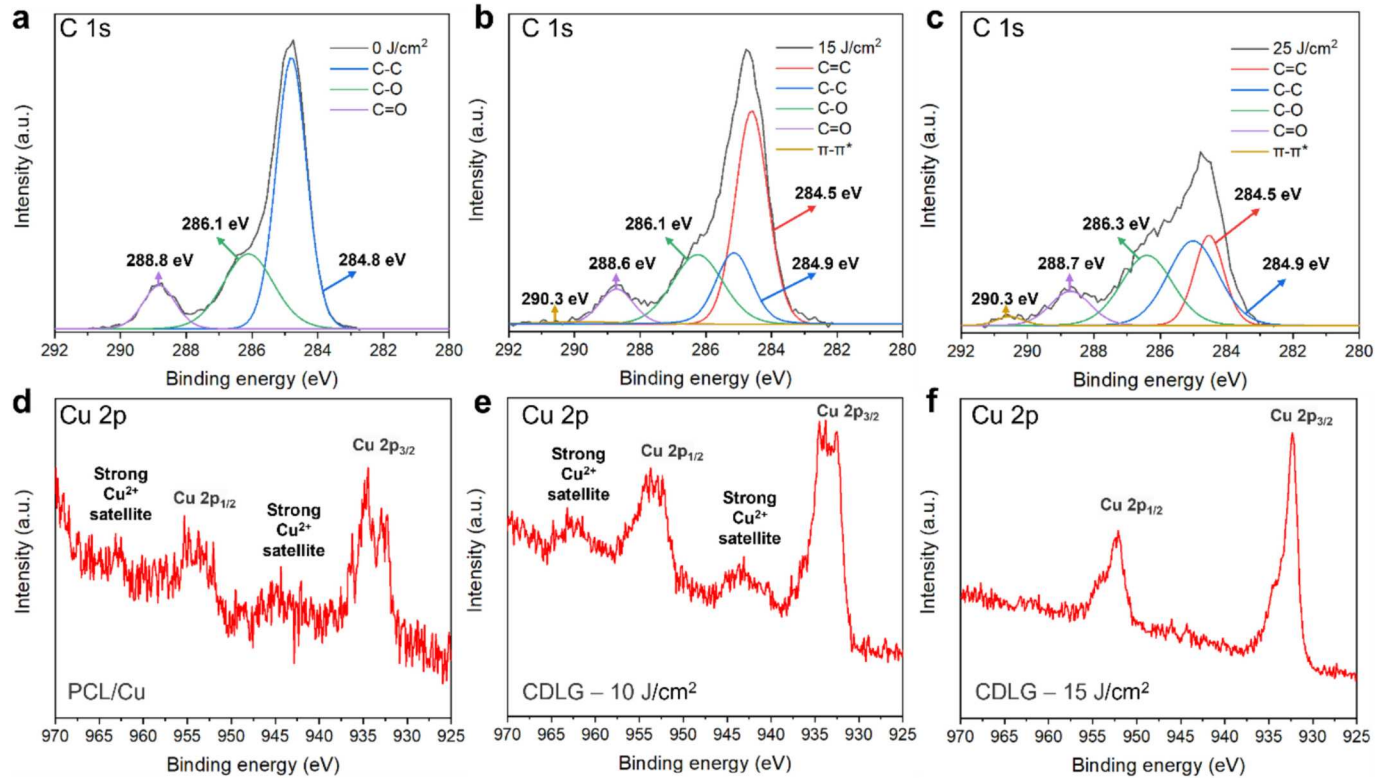

Fig. 5. C 1s XPS spectra of (a) PCL/Cu, (b) CDLG-15 J/cm^2 and (c) CDLG-25 J/cm^2; Cu 2p XPS spectra of (d) PCL/Cu, (e) CDLG-10 J/cm^2 and (f) CDLG-15 J/cm^2.

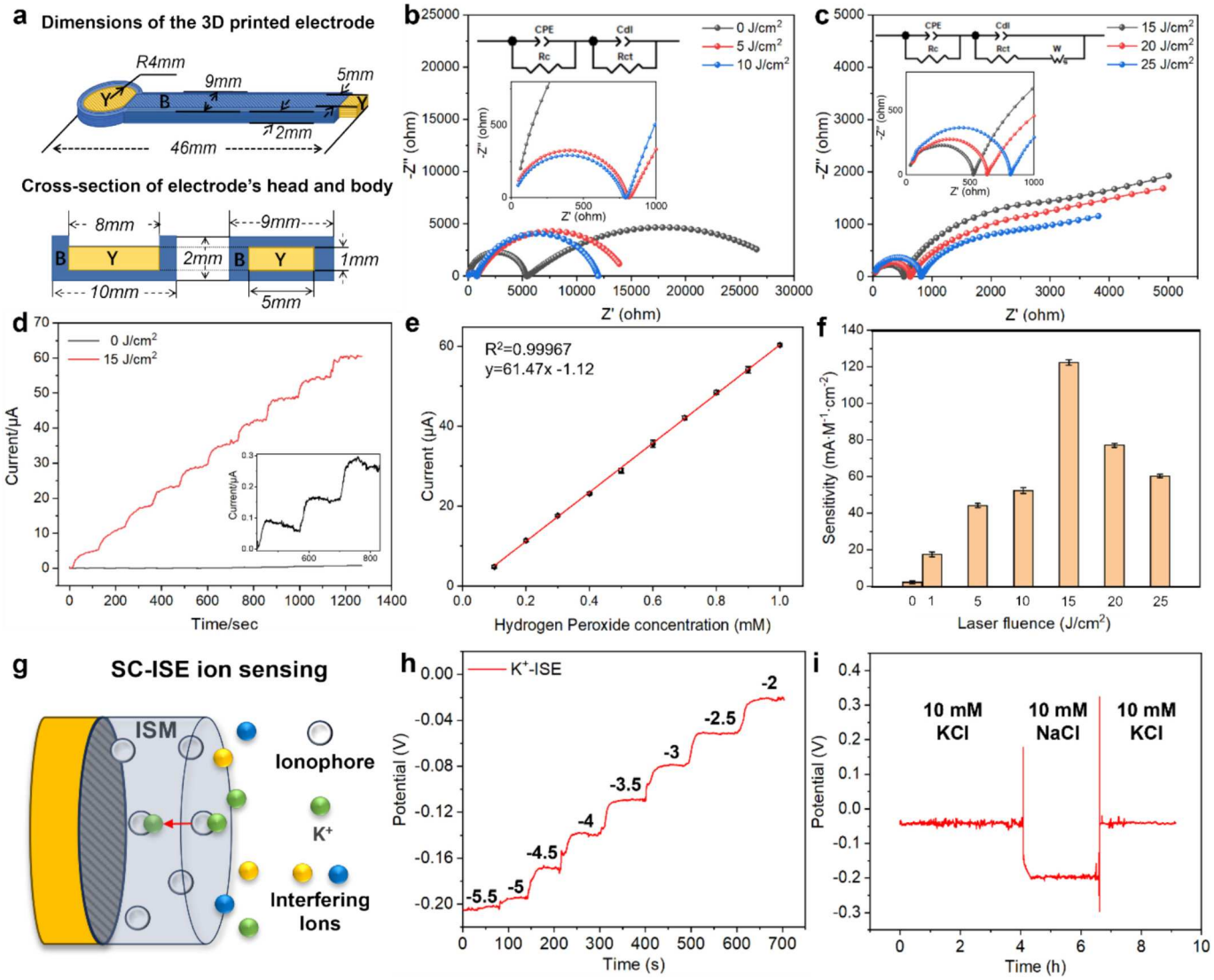

Fig. 6. (a) The designed model of the 3D printed electrode. (b) Nyquist plot and equivalent circuit derived from electrochemical impedance spectroscopy in 1× phosphate buffer solution with 0.1 mM H_2O_2 for PCL/Cu, CDLG-5 J/cm^2, CDLG-10 J/cm^2 and (c) CDLG-15 J/cm^2, CDLG-20 J/cm^2, CDLG-25 J/cm^2 3D printed electrodes. (d) Amperometric sensing of 0.1 M concentration increases (steps) of H_2O_2 with both PCL/Cu 3D printed electrode and CDLG-15 J/cm^2 3D printed electrode and (e) corresponding linear regression analysis of the current versus concentration. (f) The sensitivity of H_2O_2 with PCL/Cu 3D printed electrodes and CDLG 3D printed electrodes. (g) Illustration of SC-ISE ion sensing. (h) Open circuit potential response of the potassium ion-selective electrode (K^+ ISE). (i) The water layer test obtained upon registering the electrode response for (1) 10 mM KCl, (2) 10 mM NaCl, and (3) 10 mM KCl.

CDLG 3D-printed electrodes in 1X PBS with 0.1 mM H_2O_2. The Nyquist plots for the PCL/Cu, CDLG-5 J/cm^2, and CDLG-10 J/cm^2 3D-printed electrodes (Fig. 6b) exhibit two semi-circles in the high-frequency and mid-frequency regions, respectively. The first semi-circle (high frequency) corresponds to the contact resistance (R_c) from the current collector to the electrode composite, while the second semi-circle (mid-frequency) represents the charge-transfer resistance (R_{ct}) at the electrode/electrolyte interface. The curves are fitted using the electrical circuit model (inset in Fig. 6b), which includes a resistor for the R_c, double-layer capacitance (C_{dl}), a constant phase element representing a kinetics-controlled process (CPE), and a resistor for R_{ct} [65,66]. Following the conversion of PCL/Cu to CDLG, a significant reduction in R_c is observed, attributed to the decomposition and transformation of PCL into more conductive graphene through femtosecond laser treatment. Additionally, the R_{ct} progressively decreases with increasing laser fluence, not only due to the graphitization of PCL but also due to the reduction of CuO on the electrode surface [67]. As the laser fluence increases to 15 J/cm^2 and beyond (Fig. 6c), the complete reduction of CuO, coupled with the further growth of graphene/copper nanospheres, leads to an increase in the number of electrochemically active sites. At this point, the electrochemical reaction rate exceeds the diffusion rate, and the slopes in the low-frequency range begin to appear, indicating the presence of Warburg resistance (W), which reflects the ion diffusion process [66,68]. Due to the electrode surfaces being covered with nanoscale spherical particles, which leads to diffusion occurring on spherical surfaces, the Warburg diffusion curves at 15 J/cm^2 and above all exhibit slopes below 45° [69]. The corresponding circuit diagram (inset in Fig. 6c) compared to Fig. 6b, indicating that the reaction is now a diffusion-controlled process [66]. Moreover, the increased specific surface area resulting from the higher number of nanospheres facilitates more efficient accumulation and release of surface charges, reducing the overall impedance and causing the semi-circle in the low-frequency region to decrease in size.

Based on the EIS-derived R_{ct} values, the double-layer capacitance (C_{dl}), electrochemically active surface area (ECSA), and roughness factor (RF) of the bare and CDLG-treated electrodes were calculated, as

summarized in Table 1. After CDLG processing, a notable increase in C_{dl} was observed, attributed to the transformation of the PCL surface into conductive graphene. With increasing laser fluence, the reduction of surface CuO and progressive graphitization contribute to the enhanced C_{dl}. However, when the laser fluence exceeds 15 J/cm^2, the destruction of sp^2 carbon networks due to over-ablation leads to a decrease in C_{dl}. ECSA was calculated by normalizing C_{dl} with the specific capacitance (C_s) of the electrode material. For the bare electrode, C_s was referenced from literature as 103.9 μF·cm^{-2}, corresponding to a Cu/CuO interface [70]. Although this value may vary depending on the actual surface morphology, oxidation state, and composition [71], it serves as a reasonable approximation for estimating the ECSA in this context. For CDLG-treated electrodes, a theoretical value of 13.5 μF·cm^{-2} was adopted, corresponding to graphene-based materials [72]. Under these assumptions, the 15 J/cm^2 CDLG electrode exhibited the largest ECSA, nearly 60 times that of the bare electrode. RF was further calculated as the ratio of ECSA to the geometric area of the electrode (50 mm^2). The resulting RF values revealed that CDLG processing significantly increased the surface roughness, mainly due to the formation of nanoscale spherical features. This trend in RF aligns well with the surface morphology observed in the SEM analysis.

Next, amperometric sensing of H_2O_2 oxidation is performed to further evaluate the electroactive properties of the CDLG 3D printed electrodes and to demonstrate their effectiveness in electrochemical sensing and catalysis. The reduction of H_2O_2 is essential in a wide range of applications, from micro- and nanoscale propulsion of underwater vehicles to electrochemical biosensing [73,74]. In biosensing, H_2O_2 acts as an electrochemical transducer for various oxidoreductase enzymes (e.g., glucose oxidase, glutamate oxidase, lactate oxidase, and alcohol oxidase) in the presence of oxygen. Consequently, the electrochemical detection of H_2O_2 is critical to the functionality of numerous enzyme-based biosensors. The reduction of H_2O_2 on the PCL/Cu and CDLG 15 J/cm^2 3D-printed electrodes are investigated using CV in the presence of 0.1 mM H_2O_2 in phosphate-buffered saline (PBS) at pH 7.4(Fig. S10). A comparison of the CVs before and after the addition of 0.1 mM H_2O_2 shows that the cathodic current exhibits a slight shift at the CDLG 15 J/cm^2 3D-printed electrode, while no noticeable change is observed for the PCL/Cu 3D-printed electrode. This shift, occurring at low potentials around −0.1 V vs. Ag/AgCl, can be attributed to the onset of Faradaic current associated with H_2O_2 reduction, which induces a minor baseline displacement [75]. This analysis serves to identify an appropriate operating potential for subsequent amperometric detection of H_2O_2, with −0.1 V selected as the applied voltage due to its sensitive and stable current response.

Similarly, as shown in Fig. 6d, the comparative analysis reveals a significant enhancement in sensitivity for H_2O_2 detection in PBS on the CDLG-15 J/cm^2 3D-printed electrode compared to the PCL/Cu 3D-printed electrode. The sensitivity was calculated based on the geometric area of the electrode (50 mm^2), using the slope of the linear calibration curve obtained from the current response versus H_2O_2 concentration. The weak response currents on the PCL/Cu electrode can be attributed to the presence of copper oxide, which has a reducing effect on hydrogen peroxide. After laser scribing, it becomes evident that upon the addition of H_2O_2, the response current of the CDLG 3D-printed electrode rapidly increases and stabilizes at steady-state values. The sensitivity for H_2O_2 oxidation increases approximately sixtyfold, from 2.14 mA·M^{-1}·cm^{-2} on the PCL/Cu 3D-printed electrode to 122.9 mA·M^{-1}·cm^{-2} on the CDLG-15 J/cm^2 3D-printed electrode. This enhancement is consistent with the ECSA analysis presented in Table 1, where the ECSA of the CDLG-15 J/cm^2 electrode was estimated to be nearly 60 times greater than that of the bare PCL/Cu surface. This finding indicates that the CDLG process significantly improves electrode sensitivity by increasing the number of electroactive sites available for the redox reaction. And the sensitivity obtained from this work is significantly higher than those reported in other FDM 3D-printed electrodes for H_2O_2 detection. For example, sensors fabricated using graphene/PLA filaments with Prussian Blue surface modification have demonstrated sensitivities of 57.3 mA·M^{-1}·cm^{-2} [76] and 87 mA·M^{-1}·cm^{-2} [77], respectively. Furthermore, the plot representing the current versus H_2O_2 concentration for the CDLG-15 J/cm^2 electrode (Fig. 6e) demonstrates a linear relationship within the range of 0.1 to 1 mM, with a high correlation coefficient of $R^2 = 0.99967$. Although the graphene produced by CDLG is relatively small in size, the experimental results demonstrate that it still possesses excellent electrochemical activity.

Fig. 6f illustrates the trend in sensitivity for H_2O_2 detection using all PCL/Cu and CDLG 3D-printed electrodes. It is clear that the femtosecond laser-induced surface morphology and the transformation of PCL into graphene significantly enhance the detection of hydrogen peroxide. The highest sensitivity is achieved at a laser fluence of 15 J/cm^2, where CuO on the surface is completely reduced and graphene is not subjected to over-ablation. The changes in geometric surface roughness induced by CDLG treatment may also contribute to enhanced sensitivity. According to SEM analysis, surfaces treated at 15–25 J/cm^2 exhibit increased roughness due to the formation of a greater number of graphene-wrapped nanospherical particles on the surface. This increased roughness enhances the specific surface area. Undoubtedly, the enlarged surface area exposes more electrochemically active sites, as evidenced by the ECSA and RF values calculated in Table 1. The higher density of active sites contributes to the improved sensitivity observed in CDLG electrodes treated at higher laser fluences. These findings confirm that both the morphological and material transformations induced by CDLG synergistically enhance the electrochemical sensitivity of the electrodes. Furthermore, the stability of the CDLG-15 J/cm^2 3D-printed electrode is investigated by storing it at room temperature for over two weeks, by measuring the current response of 1 mM H_2O_2 in PBS. The current responses remain above 87 % of their initial values as shown in Fig. S11, verifying the great stability of the proposed electrode for H_2O_2 detection.

Beyond H_2O_2 detection, this device also explores the fabrication of solid-contact ISEs for K^+ detection. Potassium is a vital macronutrient essential for plant growth, soil fertility, and crop yield. Therefore, rapid and accurate detection of K^+ levels is crucial for precision agriculture and environmental monitoring applications. The potassium ISE operates based on the selective permeability of its valinomycin-based membrane, which facilitates K^+ transport while excluding other ions, as shown in Fig. 6g. The open-circuit potential response of the ISE to KCl solutions ranging from $10^{-5.5}$ M to 10^{-2} M is recorded in deionized water, exhibiting near-Nernstian behavior with a sensitivity of 54.22 mV/dec (Fig. 6h). The limit of detection (LOD) calculated by the equation LOD = 3S/N [78], is determined to be $10^{-4.82}$ M. To evaluate the long-term stability and interfacial reliability of the SC-ISE, a water layer test was performed, as shown in Fig. 6i. In this test, the sensor was immersed in 0.01 M KCl for 4 h, then transferred to 0.01 M NaCl for 2 h, and finally reintroduced into 0.01 M KCl for 2 h. This protocol allows investigation of both the formation of water layers at the membrane/solid-contact interface and the reversibility of the sensor response upon ionic strength changes [79]. Throughout the test, the electrode exhibited a minor potential drift (~0.53 mV/h) and returned to a stable baseline after re-immersion in KCl, indicating excellent interfacial adhesion and minimal water layer interference. Notably, no significant potential hysteresis or memory effects were observed, which confirms the good

Table 1
Variation of Cdl, ECSA, and RF of CDLG electrodes with increasing laser fluence.

Laser fluence (J/cm^2)	C_{dl} (μF)	ECSA (cm^2)	RF
0	30.7	0.29	0.58
1	42.8	3.17	6.34
5	93.4	6.92	13.84
10	114	8.44	16.88
15	189	14	28
20	159	11.78	23.56
25	155	11.48	22.96

reversibility and selectivity of the sensor even after ion depletion and reintroduction. These results support the robustness of the SC-ISE configuration and the viability of the 3D-printed platform for real-time environmental or agricultural ion sensing.

In practical applications, the integration of 3D printing's creative potential with the CDLG process offers significant advantages in simplifying the fabrication of complex electronic devices, particularly through device integration. This capability enables the production of multifunctional, compact systems tailored to specific applications. For example, the development of an electrochemical sensor device is demonstrated. As shown in Fig. 7a as well as the top-left corner of the image of Fig. 7b, a fully FDM 3D-printed electrochemical sensor device is displayed. The overall structure of the device forms a container designed to hold the test solution. Channels run through the walls of the container to facilitate the transfer of the test liquid into the container. At the bottom of the container, three exposed electrodes are present, serving as the working electrode, reference electrode, and counter electrode for detecting the target substance. Both the working and counter electrodes undergo CDLG surface modification after 3D printing to facilitate the detection of electrochemical reactions and the closure of the circuit, respectively. The reference electrode is coated with Ag/AgCl paste to establish a stable potential difference with the working electrode. After 3D printing and electrode surface modification, the top of the container is sealed to form an enclosed structure. The device's side channels are then used to extract the test solution into the container. The schematic of the measurement setup, which integrates a 3D-printed sensor directly coupled with a portable smartphone potentiostat, is shown in Fig. 7b.

The detection results are evaluated through chronoamperometric and potentiometric measurements using a smartphone-integrated application. For H_2O_2 detection, the current increases linearly with the H_2O_2 concentration in the range of 0–300 μM (Fig. 7c), with a correlation coefficient (R^2) of 0.9864. The LOD is determined to be 35.22 μM based on the calibration curve. Finally, we test the fabricated ion-selective device for K^+ in PBS by preparing five different samples with varying concentrations using PBS powder of different weights. The devices are used for repeated measurements to estimate the concentrations. As shown in Fig. 7d, the detection results closely match the target sample concentrations, with no interference from other ions such as Na^+. These works underscore the versatility and integration potential of 3D-printed sensors, demonstrating how FDM and CDLG techniques streamline the fabrication of compact, user-friendly devices for applications in diagnostics, environmental monitoring, and beyond.

4. Conclusion

In summary, we fabricated PCL/Cu composite electrodes through 3D printing and enhanced their electrochemical activity by modifying the electrode surface with CDLG for effective H_2O_2 and K^+ detection. With increasing laser fluence, the CDLG-modified electrode surfaces formed an increasing number of nanoscale graphene/Cu spherical particles. Further analysis using Raman, EDS, and XPS confirmed that at a laser fluence of 15 J/cm^2, a greater quantity of graphene formed and deposited on the nanoscale copper spheres, while copper oxide was reduced to copper. However, beyond this fluence, the graphene began to ablate. For H_2O_2 detection, the CDLG-modified electrode at 15 J/cm^2 exhibited a highly linear response to H_2O_2 concentration gradients, achieving a sensitivity of 122.9 mA·M^{-1}·cm^{-2}—nearly 60 times greater

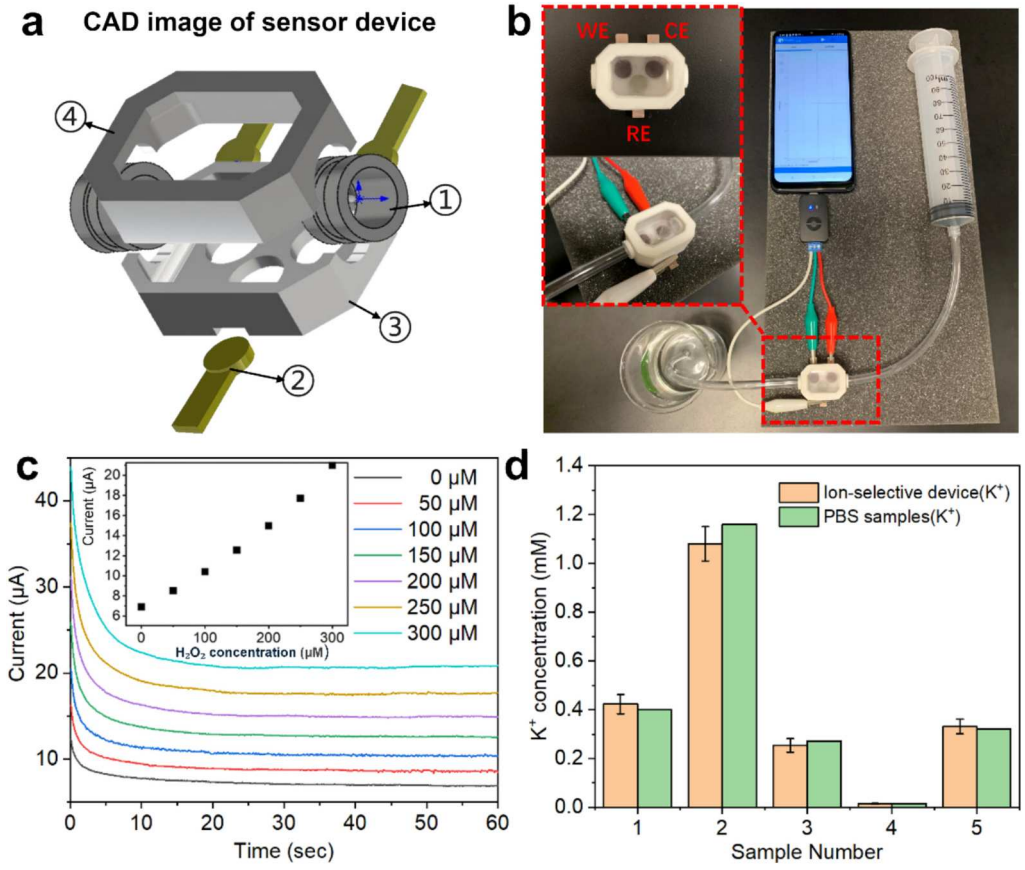

Fig. 7. (a) CAD images of the sensor device consist of two fluidic channels (1), three electrodes (2), a lower container section (3), and an upper container section (4). (b) Schematic of the measurement using 3D-printed sensor device directly coupled with a portable smartphone potentiostat. (c) Amperograms of different H_2O_2 concentrations (0–300 μM) in PBS (pH 7.4) in the 3D-printed sensor device at a potential of −0.1 V for 60 s, and a linear plot of the H_2O_2 concentration versus the current response. (d) K^+ ion detection in PBS.

than that of the unmodified electrode. After being fabricated into an ISE, the CDLG-modified electrode exhibited near-Nernstian behavior for K^+ detection, with a sensitivity of 54.22 mV/dec. Furthermore, the digitally encapsulated electrochemical device with CDLG surface modification can be coupled with a portable smartphone potentiostat, enabling convenient application. It exhibited a good linear response for H_2O_2 detection. Additionally, when configured as a K^+ ion selective device, it demonstrated reliable potassium sensing performance even in the presence of interfering ions. This research undoubtedly will broaden the horizons for 3D-printed electrochemical sensor fabrication, emphasizing the potential of combining efficient, cost-effective digital fabrication with advanced surface modifications to enhance device integration for diverse applications.

CRediT authorship contribution statement

Yan Dou: Writing – review & editing, Writing – original draft, Visualization, Validation, Software, Methodology, Investigation, Formal analysis, Data curation, Conceptualization. **Kewei Li:** Writing – review & editing, Writing – original draft, Visualization, Validation, Software, Methodology, Investigation, Formal analysis, Data curation, Conceptualization. **Haofan Sun:** Writing – review & editing, Writing – original draft, Methodology. **Kun Bi:** Writing – review & editing, Writing – original draft, Methodology. **Chenyang Zhu:** Writing – review & editing, Writing – original draft, Methodology. **Zuanyu Chen:** Methodology, Writing – original draft, Writing – review & editing. **Kailong Jin:** Methodology, Writing – original draft, Writing – review & editing. **Wonmo Kang:** Writing – review & editing, Writing – original draft, Methodology. **Xin Zhao:** Writing – review & editing, Writing – original draft, Validation, Supervision, Project administration, Methodology, Investigation, Funding acquisition, Formal analysis, Conceptualization. **Qiong Nian:** Writing – review & editing, Writing – original draft, Validation, Supervision, Project administration, Methodology, Investigation, Funding acquisition, Formal analysis, Conceptualization.

Declaration of competing interest

The authors declare the following financial interests/personal relationships which may be considered as potential competing interests: Qiong Nian reports financial support was provided by National Science Foundation. If there are other authors, they declare that they have no known competing financial interests or personal relationships that could have appeared to influence the work reported in this paper.

Acknowledgements

This study is partially supported by NSF grant CMMI-2406730, CMMI-2047000 and SRP grant FP00043048 (managers: Jeff Shaver, Matt Bregar, Madeleine Topel, and Olivia Ray). We acknowledge the use of facilities within the Eyring Materials Center at Arizona State University supported in part by NNCI-ECCS-1542160. The authors thank Dr. Martha (Molly) McCartney and Dr. David Smith for assistance with electron microscopy.

Appendix A. Supplementary data

Supplementary data to this article can be found online at https://doi.org/10.1016/j.cej.2025.168944.

Data availability

The data that has been used is confidential.

References

[1] T.C.d.O. Cândido, D.N.d. Silva, M.M.C. Borges, T.G. Barbosa, S.O.D.d. Trindade, A. C. Pereira, 3D-printed electrochemical sensors: a comprehensive review of clinical analysis applications, Analytica 5 (4) (2024) 552–575.
[2] M.N. Nadagouda, M. Ginn, V. Rastogi, A review of 3D printing techniques for environmental applications, Curr. Opin. Chem. Eng. 28 (2020) 173–178.
[3] G.L. Goh, M.F. Tay, J.M. Lee, J.S. Ho, L.N. Sim, W.Y. Yeong, T.H. Chong, Potential of printed electrodes for electrochemical impedance spectroscopy (EIS): toward membrane fouling detection, Adv. Electron. Mater. 7 (10) (2021) 2100043.
[4] A. Abdalla, B.A. Patel, 3D printed electrochemical sensors, Annu. Rev. Anal. Chem. 14 (1) (2021) 47–63.
[5] R.M. Cardoso, C. Kalinke, R.G. Rocha, P.L. Dos Santos, D.P. Rocha, P.R. Oliveira, B. C. Janegitz, J.A. Bonacin, E.M. Richter, R.A. Munoz, Additive-manufactured (3D-printed) electrochemical sensors: a critical review, Anal. Chim. Acta 1118 (2020) 73–91.
[6] A. Sharma, H. Faber, A. Khosla, T.D. Anthopoulos, 3D printed electrochemical devices for bio-chemical sensing: a review, Mater. Sci. Eng. R. Rep. 156 (2023) 100754.
[7] P.A. Ferreira, F.M. de Oliveira, E.I. de Melo, A.E. de Carvalho, B.G. Lucca, V. S. Ferreira, R.A.B. da Silva, Multi sensor compatible 3D-printed electrochemical cell for voltammetric drug screening, Anal. Chim. Acta 1169 (2021) 338568.
[8] A. Baltima, H. Panagopoulou, A. Economou, C. Kokkinos, 3D-printed fluidic electrochemical microcell for sequential injection/stripping analysis of heavy metals, Anal. Chim. Acta 1159 (2021) 338426.
[9] V. Katseli, A. Economou, C. Kokkinos, Smartphone-addressable 3D-printed electrochemical ring for nonenzymatic self-monitoring of glucose in human sweat, Anal. Chem. 93 (7) (2021) 3331–3336.
[10] A. Ainla, M.P. Mousavi, M.-N. Tsaloglou, J. Redston, J.G. Bell, M.T. Fernández-Abedul, G.M. Whitesides, Open-source potentiostat for wireless electrochemical detection with smartphones, Anal. Chem. 90 (10) (2018) 6240–6246.
[11] J. Yang, Y. Cheng, X. Gong, S. Yi, C.-W. Li, L. Jiang, C. Yi, An integrative review on the applications of 3D printing in the field of in vitro diagnostics, Chin. Chem. Lett. 33 (5) (2022) 2231–2242.
[12] Y. Xu, X. Wu, X. Guo, B. Kong, M. Zhang, X. Qian, S. Mi, W. Sun, The boom in 3D-printed sensor technology, Sensors 17 (5) (2017) 1166.
[13] J. Muñoz, M. Pumera, Accounts in 3D-printed electrochemical sensors: towards monitoring of environmental pollutants, ChemElectroChem 7 (16) (2020) 3404–3413.
[14] M.R. Khosravani, T. Reinicke, 3D-printed sensors: current progress and future challenges, Sensors Actuators A Phys. 305 (2020) 111916.
[15] Y. Ni, R. Ji, K. Long, T. Bu, K. Chen, S. Zhuang, A review of 3D-printed sensors, Appl. Spectrosc. Rev. 52 (7) (2017) 623–652.
[16] C.W. Foster, H.M. Elbardisy, M.P. Down, E.M. Keefe, G.C. Smith, C.E. Banks, Additively manufactured graphitic electrochemical sensing platforms, Chem. Eng. J. 381 (2020) 122343.
[17] K. Gnanasekaran, T. Heijmans, S. Van Bennekom, H. Woldhuis, S. Wijnia, G. De With, H. Friedrich, 3D printing of CNT-and graphene-based conductive polymer nanocomposites by fused deposition modeling, Appl. Mater. Today 9 (2017) 21–28.
[18] S. Kwok, K. Goh, Z. Tan, S. Tan, W. Tjiu, J. Soh, Z. Ng, Y. Chan, H. Hui, K. Goh, Electrically conductive filament for 3D-printed circuits and sensors, Appl. Mater. Today 9 (2017) 167–175.
[19] H. Wei, X. Cauchy, I.O. Navas, Y. Abderrafai, K. Chizari, U. Sundararaj, Y. Liu, J. Leng, D. Therriault, Direct 3D printing of hybrid nanofiber-based nanocomposites for highly conductive and shape memory applications, ACS Appl. Mater. Interfaces 11 (27) (2019) 24523–24532.
[20] S. Agarwala, G.L. Goh, G.D. Goh, V. Dikshit, W.Y. Yeong, 3D and 4D printing of polymer/CNTs-based conductive composites, in: 3D and 4D Printing of Polymer Nanocomposite Materials, 2020, pp. 297–324.
[21] J.S. Stefano, C. Kalinke, R.G. da Rocha, D.P. Rocha, V.A.O.P. da Silva, J.A. Bonacin, L. Angnes, E.M. Richter, B.C. Janegitz, R.A.A. Muñoz, Electrochemical (bio) sensors enabled by fused deposition modeling-based 3D printing: a guide to selecting designs, printing parameters, and post-treatment protocols, ACS Publ. 94 (17) (2022) 6417–6636.
[22] S.W. Kwok, K.H.H. Goh, Z.D. Tan, S.T.M. Tan, W.W. Tjiu, J.Y. Soh, Z.J.G. Ng, Y. Z. Chan, H.K. Hui, K.E.J. Goh, Electrically conductive filament for 3D-printed circuits and sensors, Appl. Mater. Today 9 (2017) 167–175.
[23] P.F. Flowers, C. Reyes, S. Ye, M.J. Kim, B.J. Wiley, 3D printing electronic components and circuits with conductive thermoplastic filament, Addit. Manuf. 18 (2017) 156–163.
[24] J. Tan, H. Low, Embedded electrical tracks in 3D printed objects by fused filament fabrication of highly conductive composites, in: Addit Manuf 23: 294–302, ed, 2018.
[25] T.H. Lim, S.H. Lee, S.Y. Yeo, Highly conductive polymer/metal/carbon nanotube composite fiber prepared by the melt-spinning process, Text. Res. J. 87 (5) (2017) 593–606.
[26] M.A. Cruz, S. Ye, M.J. Kim, C. Reyes, F. Yang, P.F. Flowers, B.J. Wiley, Multigram synthesis of Cu-Ag core–shell nanowires enables the production of a highly conductive polymer filament for 3D printing electronics, Part. Part. Syst. Charact. 35 (5) (2018) 1700385.
[27] R.M. Cardoso, P.R. Silva, A.P. Lima, D.P. Rocha, T.C. Oliveira, T.M. do Prado, E. L. Fava, O. Fatibello-Filho, E.M. Richter, R.A. Muñoz, 3D-printed graphene/polylactic acid electrode for bioanalysis: biosensing of glucose and simultaneous determination of uric acid and nitrite in biological fluids, Sensors Actuators B Chem. 307 (2020) 127621.

[28] F. Novotný, V. Urbanová, J. Plutnar, M. Pumera, Preserving fine structure details and dramatically enhancing electron transfer rates in graphene 3D-printed electrodes via thermal annealing: toward nitroaromatic explosives sensing, ACS Appl. Mater. Interfaces 11 (38) (2019) 35371–35375.
[29] J.F. Pereira, R.G. Rocha, S.V. Castro, A.F. Joao, P.H. Borges, D.P. Rocha, A. de Siervo, E.M. Richter, E. Nossol, R.V. Gelamo, Reactive oxygen plasma treatment of 3D-printed carbon electrodes towards high-performance electrochemical sensors, Sensors Actuators B Chem. 347 (2021) 130651.
[30] G.L. Goh, S. Agarwala, Y.J. Tan, W.Y. Yeong, A low cost and flexible carbon nanotube pH sensor fabricated using aerosol jet technology for live cell applications, Sensors Actuators B Chem. 260 (2018) 227–235.
[31] E. Cantù, S. Tonello, G. Abate, D. Uberti, E. Sardini, M. Serpelloni, Aerosol jet printed 3D electrochemical sensors for protein detection, Sensors 18 (11) (2018) 3719.
[32] Y. Dou, R. Dai, H. Sun, K. Bi, X. Zhao, Q. Nian, Reduced graphene oxide-modified electrodes via fused deposition modeling 3D printing for hydrogen peroxide sensor, 2D Mater. 11 (4) (2024) 045008.
[33] L. Cançado, K. Takai, T. Enoki, M. Endo, Y. Kim, H. Mizusaki, A. Jorio, L. Coelho, R. Magalhães-Paniago, M. Pimenta, General equation for the determination of the crystallite size La of nanographite by Raman spectroscopy, Appl. Phys. Lett. 88 (16) (2006).
[34] X. Jia, X. Zhao, Numerical study of material decomposition in ultrafast laser interaction with metals, Appl. Surf. Sci. 463 (2019) 781–790.
[35] S. Zhang, Y.C. Shin, Analysis of the heat-affected zone and ablation efficiency in terms of burst mode parameters during high power picosecond laser micromachining of metals, J. Manuf. Sci. Eng. 145 (4) (2023) 041006.
[36] T. Elzein, M. Nasser-Eddine, C. Delaite, S. Bistac, P. Dumas, FTIR study of polycaprolactone chain organization at interfaces, J. Colloid Interface Sci. 273 (2) (2004) 381–387.
[37] R. Ye, D.K. James, J.M. Tour, Laser-induced graphene, Acc. Chem. Res. 51 (7) (2018) 1609–1620.
[38] J. Lin, Z. Peng, Y. Liu, F. Ruiz-Zepeda, R. Ye, E.L. Samuel, M.J. Yacaman, B. I. Yakobson, J.M. Tour, Laser-induced porous graphene films from commercial polymers, Nat. Commun. 5 (1) (2014) 5714.
[39] R. Ye, Y. Chyan, J. Zhang, Y. Li, X. Han, C. Kittrell, J.M. Tour, Laser-induced graphene formation on wood, Adv. Mater. 29 (37) (2017) 1702211.
[40] Y. Chyan, R. Ye, Y. Li, S. Singh, C. Arnusch, J. Tour, Laser-induced graphene by multiple lasing: toward electronics on cloth, paper, and food, ACS Nano 12 (2018) 2176–2183.
[41] S.M. Eaton, H. Zhang, P.R. Herman, F. Yoshino, L. Shah, J. Bovatsek, A.Y. Arai, Heat accumulation effects in femtosecond laser-written waveguides with variable repetition rate, Opt. Express 13 (12) (2005) 4708–4716.
[42] M. Terakawa, Femtosecond laser processing of biodegradable polymers, Appl. Sci. 8 (7) (2018) 1123.
[43] A. Semerok, B. Salle, J.-F. Wagner, G. Petite, Femtosecond, picosecond, and nanosecond laser microablation: laser plasma and crater investigation, Laser Part. Beams 20 (1) (2002) 67–72.
[44] K.K. Garg, S. Pandey, L. Pandey, A. Kumar, A. Rana, S. Madan, N.G. Sahoo, S. Dhawan, R.K. Singh, Copper-catalyzed plastic waste synthesized graphene nanosheets/polypyrrole nanocomposites for efficient thermoelectric applications, Next Sustain. 5 (2025) 100081.
[45] D. Boyd, W.-H. Lin, C.-C. Hsu, M. Teague, C.-C. Chen, Y.-Y. Lo, W.-Y. Chan, W.-B. Su, T.-C. Cheng, C.-S. Chang, Single-step deposition of high-mobility graphene at reduced temperatures, Nat. Commun. 6 (1) (2015) 6620.
[46] J. Jang, M. Son, S. Chung, K. Kim, C. Cho, B.H. Lee, M.-H. Ham, Low-temperature-grown continuous graphene films from benzene by chemical vapor deposition at ambient pressure, Sci. Rep. 5 (1) (2015) 17955.
[47] M. Saeed, Y. Alshammari, S.A. Majeed, E. Al-Nasrallah, Chemical vapour deposition of graphene—synthesis, characterisation, and applications: a review, Molecules 25 (17) (2020) 3856.
[48] S. Pekdemir, M.S. Onses, M. Hancer, Low temperature growth of graphene using inductively-coupled plasma chemical vapor deposition, Surf. Coat. Technol. 309 (2017) 814–819.
[49] J.-H. Choi, Z. Li, P. Cui, X. Fan, H. Zhang, C. Zeng, Z. Zhang, Drastic reduction in the growth temperature of graphene on copper via enhanced London dispersion force, Sci. Rep. 3 (1) (2013) 1925.
[50] M. Pimenta, G. Dresselhaus, M.S. Dresselhaus, L. Cancado, A. Jorio, R. Saito, Studying disorder in graphite-based systems by Raman spectroscopy, Phys. Chem. Chem. Phys. 9 (11) (2007) 1276–1290.
[51] P. Wu, W. Zhang, Z. Li, J. Yang, Mechanisms of graphene growth on metal surfaces: theoretical perspectives, Small 10 (11) (2014) 2136–2150.
[52] B. Qing-Shun, D. Yu-Hao, H. Xin, Z. Ai-Min, G. Yong-Bo, Deposition and growth mechanism of graphene on copper crystal surface based on molecular dynamics simulation, Acta Phys. Sin. 69 (22) (2020).
[53] Q. Li, J. Luo, Z. Li, M.H. Rummeli, L. Liu, Density functional theory and molecular dynamics study on the growth of graphene by chemical vapor deposition on copper substrate, J. Vac. Sci. Technol. A 42 (4) (2024).
[54] H.C. Hong, J.I. Ryu, H.C. Lee, Recent understanding in the chemical vapor deposition of multilayer graphene: controlling uniformity, thickness, and stacking configuration, Nanomaterials 13 (15) (2023) 2217.
[55] C.-H. Lu, K.-M. Shang, S.-R. Lee, C.-M. Leu, Y.-C. Tai, N.-C. Yeh, Low-temperature direct growth of nanocrystalline multilayer graphene on silver with long-term surface passivation, ACS Appl. Mater. Interfaces 15 (7) (2023) 9883–9891.
[56] M.D. Bhatt, H. Kim, G. Kim, Various defects in graphene: a review, RSC Adv. 12 (33) (2022) 21520–21547.
[57] I. Gnilitskyi, S. Bellucci, A.G. Marrani, M. Shepida, A. Mazur, G. Zozulya, V. Kordan, V. Babizhetskyy, B. Sahraoui, O. Kuntyi, Femtosecond laser-induced nano-and microstructuring of Cu electrodes for CO2 electroreduction in acetonitrile medium, Sci. Rep. 13 (1) (2023) 8837.
[58] O. Koritsoglou, G. Duchateau, O. Utéza, A. Mouskeftaras, Quantitative assessment of femtosecond laser-induced stress waves in fused silica, Phys. Rev. B 110 (5) (2024) 054112.
[59] M. Liu, J. Wu, H. Cheng, Effects of laser processing parameters on properties of laser-induced graphene by irradiating CO2 laser on polyimide, SCIENCE CHINA Technol. Sci. 65 (1) (2022) 41–52.
[60] Y. Wei, W. Li, S. Zhang, J. Yu, Y. Tang, J. Wu, S. Yu, Laser-induced porous graphene/CuO composite for efficient interfacial solar steam generation, Adv. Funct. Mater. 34 (28) (2024) 2401149.
[61] A.K. Geim, Graphene: status and prospects, science 324 (5934) (2009) 1530–1534.
[62] R. Al-Gaashani, A. Najjar, Y. Zakaria, S. Mansour, M. Atieh, XPS and structural studies of high quality graphene oxide and reduced graphene oxide prepared by different chemical oxidation methods, Ceram. Int. 45 (11) (2019) 14439–14448.
[63] A. Morais, J.P.C. Alves, F.A.S. Lima, M. Lira-Cantu, A.F. Nogueira, Enhanced photovoltaic performance of inverted hybrid bulk-heterojunction solar cells using TiO 2/reduced graphene oxide films as electron transport layers, J. Photon. Energ. 5 (1) (2015) 057408.
[64] J.-U. Lee, J.-h. Lee, C.-W. Lee, S.-C. Cho, S.-M. Hong, Y.-w. Ma, S.-Y. Jeong, B.-S. Shin, Green synthesis of laser-induced graphene with copper oxide nanoparticles for deicing based on photo-electrothermal effect, Nanomaterials 12 (6) (2022) 960.
[65] M. Xu, H.D. Dewald, Impedance studies of copper foil and graphite-coated copper foil electrodes in lithium-ion battery electrolyte, Electrochim. Acta 50 (27) (2005) 5473–5478.
[66] A.J. Bard, L.R. Faulkner, H.S. White, Electrochemical Methods: Fundamentals and Applications, John Wiley & Sons, 2022.
[67] A.R. Bredar, A.L. Chown, A.R. Burton, B.H. Farnum, Electrochemical impedance spectroscopy of metal oxide electrodes for energy applications, ACS Appl. Energy Mater. 3 (1) (2020) 66–98.
[68] P. Zanello, C. Nervi, F.F. De Biani, Inorganic electrochemistry: theory, practice and application, Roy. Soc. Chem. (2019).
[69] H.-C. Yu, S.B. Adler, S.A. Barnett, K. Thornton, Simulation of the diffusional impedance and application to the characterization of electrodes with complex microstructures, Electrochim. Acta 354 (2020) 136534.
[70] B. Wang, B. Cao, C. Wang, Y. Zhang, H. Yao, Y. Wang, The optical and electrical performance of CuO synthesized by anodic oxidation based on copper foam, Materials 13 (23) (2020) 5411.
[71] V. Senthilkumar, Y.S. Kim, S. Chandrasekaran, B. Rajagopalan, E.J. Kim, J. S. Chung, Comparative supercapacitance performance of CuO nanostructures for energy storage device applications, RSC Adv. 5 (26) (2015) 20545–20553.
[72] H. Ji, X. Zhao, Z. Qiao, J. Jung, Y. Zhu, Y. Lu, L.L. Zhang, A.H. MacDonald, R. S. Ruoff, Capacitance of carbon-based electrical double-layer capacitors, Nat. Commun. 5 (1) (2014) 3317.
[73] K.M. Marr, B. Chen, E.J. Mootz, J. Geder, M. Pruessner, B.J. Melde, R.R. Vanfleet, I. L. Medintz, B.D. Iverson, J.C. Claussen, High aspect ratio carbon nanotube membranes decorated with Pt nanoparticle urchins for micro underwater vehicle propulsion via H2O2 decomposition, ACS Nano 9 (8) (2015) 7791–7803.
[74] Q. Rui, K. Komori, Y. Tian, H. Liu, Y. Luo, Y. Sakai, Electrochemical biosensor for the detection of H2O2 from living cancer cells based on ZnO nanosheets, Anal. Chim. Acta 670 (1–2) (2010) 57–62.
[75] A. Zöpfl, M. Sisakthi, J. Eroms, F.-M. Matysik, C. Strunk, T. Hirsch, Signal enhancement in amperometric peroxide detection by using graphene materials with low number of defects, Microchim. Acta 183 (2016) 83–90.
[76] R.G. Rocha, J.S. Stefano, R.M. Cardoso, P.J. Zambiazi, J.A. Bonacin, E.M. Richter, R.A. Munoz, Electrochemical synthesis of Prussian blue from iron impurities in 3D-printed graphene electrodes: amperometric sensing platform for hydrogen peroxide, Talanta 219 (2020) 121289.
[77] V. Katic, P.L. Dos Santos, M.F. Dos Santos, B.M. Pires, H.C. Loureiro, A.P. Lima, J. C. Queiroz, R. Landers, R.A. Muñoz, J.A. Bonacin, 3D printed graphene electrodes modified with prussian blue: emerging electrochemical sensing platform for peroxide detection, ACS Appl. Mater. Interfaces 11 (38) (2019) 35068–35078.
[78] J. Vial, A. Jardy, Experimental comparison of the different approaches to estimate LOD and LOQ of an HPLC method, Anal. Chem. 71 (14) (1999) 2672–2677.
[79] D. Rojas, D. Torricelli, M. Cuartero, G.A. Crespo, 3D-printed transducers for solid contact potentiometric ion sensors: improving reproducibility by fabrication automation, Anal. Chem. 96 (39) (2024) 15572–15580.